Lawrence Berkeley National Laboratory
Lawrence Berkeley National Laboratory

## Title
Extreme ultraviolet mask substrate surface roughness effects on lithography patterning

## Permalink
https://escholarship.org/uc/item/0n66t43w

## Author
George, Simi

## Publication Date
2010-10-06

eScholarship.org Powered by the California Digital Library
University of California

# Extreme ultraviolet mask substrate surface roughness effects on lithographic patterning

Running title: EUV mask surface cleaning effects on lithography process performance

Running Authors: George, Naulleau, Salmassi, Mochi, Gullikson, Goldberg, and Anderson

Simi A. George[a)], Patrick P. Naulleau[b)], Farhad Salmassi, Iacopo Mochi, Eric M. Gullikson, Kenneth A. Goldberg, and Erik H. Anderson

Center for X-ray Optics, Lawrence Berkeley National Laboratory, 1 Cyclotron Road, Berkeley, CA, 94720

[a)]Electronic Mail: sageorge@lbl.gov

[b)]Electronic Mail: pnaulleau@lbl.gov

Material Names: Silicon, Molybdenum, Chromium, Ruthenium

In extreme ultraviolet lithography exposure systems, mask substrate roughness induced scatter contributes to LER at the image plane. In this paper, the impact of mask substrate roughness on image plane speckle is explicitly evaluated. A programmed roughness mask was used to study the correlation between mask roughness metrics and wafer plane aerial image inspection. We find that the roughness measurements by top surface topography profile do not provide complete information on the scatter related speckle that leads to LER at the image plane. We suggest at-wavelength characterization by imaging and/or scatter measurements into different frequencies as an alternative for a more comprehensive metrology of the mask substrate/multilayer roughness effects.

## I. INTRODUCTION

Pattern resolutions of 16 nm or better are becoming the requirement for advanced lithography. The candidate technology at the forefront for high volume manufacturing (HVM) is extreme ultraviolet lithography (EUVL) [1-3]. EUV based optical projection systems utilize a patterning wavelength near 13.5 nm. Wavelengths in this region are absorbing in matter; thus, an all reflective system in vacuum is a requirement. In order to achieve high reflectivities at this illuminating wavelength, the optics and the reflective photomask[4] exploit thin film interference properties with 40 or more alternating thin layers of Molybdenum and Silicon deposited on a substrate. Further details on the theory, the architecture and the choice of materials for the mask and optics, and on the surface fabrication processes can be found in literature[2-6].

A considerable problem for the mask and the optics at this illuminating wavelength is roughness-induced multilayer scattering or non-specular scattering[5, 7, 8]. It is well known that non-specular scattering leads to throughput loss in the optical systems and to reduced image contrast. Multilayer scattering, which is considered to be fundamentally different from single surface scattering, is characterized by interference effects arising from the roughness of the different material interfaces as well as the conformal growth of the substrate roughness to the top layer surface. These interference effects, occurring at higher frequencies (hence, treated as a statistical effect) than the surface figure and finish errors, cause phase modulations in the image field (speckle) that ultimately leads to loss of fidelity in the optical system[9]. More specifically, the mask substrate roughness directly leads to LER through the formation of speckle in the patterned image[10].

Recently updated International Technology Roadmap for Semiconductors (ITRS)[11] limits the LER in resists[12,13] to be less than 1.2nm 3σ LER at the 20nm half-pitch resolution. Under such constraints, it has recently been shown that mask contributors to LER play a significant role[13-16]. Of particular concern is the substrate roughness issue discussed above, especially as the illumination coherence is increased[17-19].

Modeling has shown that the mask multilayer roughness must be limited to 50 picometers to meet current LER targets for the 22 and 16-nm half-pitch lithography nodes[19, 20]. For EUV, the phase coherent roughness that propagates from layer to layer is considered to be significant, bringing into question the suitability of top-surface roughness analysis methods such as Atomic Force Microscopy (AFM) for its characterization. Because the root cause of LER from phase coherent roughness is speckle in the aerial image, it is crucial to understand the relationships between bottom (substrate) surface roughness, top surface roughness, EUV scattering, and aerial image speckle for developing accurate mask specifications and suitable roughness metrics.

In this paper, we explicitly study the impact of substrate roughness on image plane speckle. We quantify the extent to which an AFM measurement can be depended upon for specifying tolerable roughness limits on EUV masks and demonstrate an alternative metrology method capable of directly measuring phase-coherent roughness. Design of the study involved a mask prepared with areas of varying roughness that was then deposited with a Mo-Si multilayer. AFM based topography was collected for each area before and after multilayer deposition. The same rough areas were then subjected to EUV reflectometry and scattering measurements to obtain phase-coherent roughness parameters. These areas were then imaged at-wavelength[21]; thus, directly characterizing the aerial image speckle. Finally, modeling is used to test the effectiveness of the two different roughness metrologies in predicting the measured aerial-image speckle.

# II. MASK MULTILAYER SURFACE CHARACTERIZATIONS

The basic structure of EUV masks start with a highly polished Quartz type substrate of low thermal expansion. Forty or more alternating layers of Molybdenum (Mo) and Silicon (Si) are deposited on top of the substrate to provide high EUV reflectivity. A protective capping layer is deposited on top of the multilayer pairs and lithographic patterning is completed with a buffer/absorber stack over all of the mirror layers. For the studies completed here, we synthesize a mask like surface containing a range of starting roughness that is then coated with multilayers to obtain reflectivities typical for a standard EUV mask.

## *A. Mask Fabrication for Controlled Roughness Studies*

Since mask blanks with roughness gradients are not readily available, a mask like surface was fabricated for the measurements completed here. The fabrication procedure involved the shadowed deposition of Chromium (Cr) onto a standard 4" Silicon (Si) wafer by inductively coupled plasma assisted DC magnetron sputtering in a mixed gas environment. The shadowing was controlled in such a way that a thickness variation of the Cr deposit is created from one end of the wafer to the other and the thickness related gradation in granularities/roughness is obtained. For the metrologies completed here, we look at a row of 18 windows going from low roughness to high roughness as shown in figure 1.

**Figure 1:** A grid pattern of windows sized 1x3mm and separated by 1.5mm, going from low roughness to high roughness. There are a total of 18 windows sized 1x3mm and separated by 1.5mm in the row that was evaluated for this study. The clear multilayer surface is inside the window and resist absorber giving full attenuation of EUV is on the outside.

## *B. Surface Analysis by Atomic Force Microscopy*

Atomic force microscope (AFM) imaging of the Cr coated surface was completed at specific coordinates along the axis of increasing roughness on the wafer. Forty alternating layers of Molybdenum (Mo) and Si were then deposited on top of the sputter coated Cr surface of the wafer. A second set of AFM images were collected from the exposed multilayer surface at roughly the same coordinates as before. The instrument used for measurements is the Digital Instruments model DM 3100 scanning probe microscope developed by the Veeco metrology group. All AFM scans were completed with the Nanoscope IIIa Controller over a 5µmx5µm area, in tapping mode, and analyzed offline with the commercially available image analysis package SUMMIT[22] to determine the root mean square (rms) deviation roughness of the surfaces.

From the surface height distributions in the AFM surface profiles, the rms roughness, $\sigma = \left[ \left\langle \left( h - \langle h \rangle \right)^2 \right\rangle \right]^{1/2}$, is determined for the various roughness regions. The rms numbers tabulated for images collected before and after Mo/Si multilayer (ML) is deposited on chrome are given in table 1. After ML deposition, the minimum in the measured roughness is at 0.2nm, which gives approximately 1.9nm peak-valley (p-v) errors. We note that presently, the best EUV mask blanks roughness are characterized to be near or better than 0.2nm rms. The maximum in the roughness is found to be at 0.54nm and corresponds to nearly 5nm of p-v errors. The correlation lengths computed from the autocorrelation of the image surface heights is approximately 60nm on average for the ML coated surfaces.

**Table 1**: Roughness (root mean square deviations) computed from AFM imaged surface profiles before and after the multilayer depositions.

The tabulated rms values are plotted in figure 2 as a function of increasing region number (correlated to the increase in the chromium thickness and roughness). It is immediately obvious from the plot that there is roughness smoothing occurring in the rougher mask areas after the ML deposition. On the other hand, very little smoothing is observed at the smaller substrate roughness regions near 0.2nm. We conclude that this is due to the ML itself having intrinsic roughness and when the starting substrate roughness is too small, the smoothing effect is mitigated.

**Figure 2:** Root mean square height deviations from the AFM surface profiles of the sputter coated Chrome on Si rough mask, before and after Mo/Si multilayer coating. Rougher areas of the mask show smoothing after multilayer is deposited and at smaller roughness scales, the smoothing appears to be diminished.

To better illustrate this point, the isotropic power spectral densities (PSD) obtained for the images before and after the ML coating are compared at a roughness minimum and roughness maximum. Figure 3 shows two AFM surface measurements, specifically for mask multilayer surfaces in regions 6 and 15. The measured roughness for region 6 is 0.23nm before ML coating and 0.2nm after; and the surface in region 15 shows a reduction from 0.8nm to 0.5nm rms

roughness after ML. In looking at the PSDs generated (figure 3, top) for region 6 in the low roughness region, where the solid black curve is the PSD of the chromium surface by itself, we observe an increase in the low spatial frequency range (LSFR) and some smoothing in the mid to high spatial frequencies (MSFR and HSFR) after the ML is coated. In contrast, the PSDs for region 15 (figure 3, bottom) with taller phase structures show significant reduction into all frequencies after ML deposition. This effect is due to the smoothing induced by the ML structures. Figure 4 shows two masks (low and high roughness components) synthesized from AFM image scans to be used for the thin mask model used for predicting phase coherent roughness contributed speckle. The phase is depicted in grayscale and the phase errors are included from the PSD.

**Figure 3:** PSDs generated (window 6, top) in the low roughness region with the solid black curve is the PSD of the chromium surface by itself. An increase in the low spatial frequency range (LSFR) and some smoothing into the mid to high spatial frequencies (MSFR and HSFR) are observed after the ML is coated on this surface. In contrast, the PSD's for high roughness (window 15, bottom) show significant reduction into all frequencies after ML deposition. The taller phase structures are assumed to have been smoothed.

**Figure 4:** Images synthesized from AFM image scans to be used for the thin mask model for predicting phase coherent roughness contributed speckle.

## *C. X-ray Reflectance Measurements*

Another way to extract roughness from a surface is by using x-ray reflectance and scattering (XRS) measurements at wavelength. For this purpose, we utilized a synchrotron based reflectometer located at the advanced light source (ALS) beamline 6.3.2 of the Lawrence Berkeley National Laboratory (LBNL). The main advantage of the beamline is its high spectral purity, a spectral resolving power (eV/ΔeV) of up to 7000, a wavelength accuracy of $10^{-3}$ nm, and a reflectivity accuracy of 0.1% (absolute). The high spectral resolution is achieved by utilizing a variable line space grating. Further details of the beamline and the instrument can be found in the literature[23].

Reflectance measurements were performed at a wavelength of 13.46nm with a relative spectral bandwidth, $\lambda/\Delta \lambda$, of approximately 0.01%. The photon beam is incident on the sample surface at a 5° angle from the normal and the specular reflectance is measured at the same angle. The specular beam divergence is ± 1.2 degrees and the detector is large in comparison to reflected beam NA. The diffuse scattering from the surfaces are measured at a fixed 5°angle from the reflected beam or ten degrees away from the surface normal. The raw reflectance and scattering yields for the measurements from the different windows are shown in figure 5 on the scale of increasing roughness. Scattering measurements are obtained at a single frequency and serves to illustrate that an increase in phase roughness scatters intensity away from reflected specular beam. In figure 5, the increase in scattering is seen to follow the decrease in reflectance owing to the increase in phase roughness of the measured surfaces.

**Figure 5:** The reflectance and scattering yields for the measurements from the different windows are shown on the scale of increasing roughness. Increase in scattering follows the decrease in reflectance, indicating an increase in phase roughness. Wavelength of light used was

13.46 nm at a 5 degree angle of incidence for reflectance relative to the normal. The scattering was obtained at a fixed angle that was 10 degrees away from the normal.

In order to extract rms surface roughness from the measured reflectivities, we take advantage of the relationship between scattering and reflectance. Assuming that reflectivity is spread over the width of the interface and assuming that this width is related to the roughness of the interface; it can be represented statistically as a Gaussian. Total reflectivity is reduced because amplitudes reflected from different depths add with different phases. For an initial reflectance less than one and assuming that refraction effects are negligible the Gaussian can be Fourier transformed from coordinates to momentum transfer to obtain reflectivity reduction as a function of wavelength or angle of incidence. The momentum transfer is replaced with the multilayer period, which gets us to the Debye-Waller factor for the reduction of reflectances to which the expression for total integrated scatter, $TIS = \left(\frac{4\pi\sigma\cos\theta}{\lambda}\right)^2 = 1 - \frac{R}{R_0}$, can be related to approximate the rms roughness term. Phase roughness computed using this relationship and the measured reflectivities from the mask surface is tabulated in table 2, alongside the corresponding AFM measured roughness.

**Table 2**: RMS roughness computed from AFM imaging and the measured XRS reflectances of the rough mask windows.

In figure 6, the two sets of roughness data is plotted for comparison against the region numbers. A fixed uncertainty of 10% is assumed for both measurements. The two sets of data in figure 6 are seen to overlap where the substrate phase roughness heights are large. In the smallest substrate roughness areas, XRS determined roughness is nearly 50% lower than the AFM measured roughness values.

**Figure 6:** AFM and XRS measured rms roughness are compared. The two sets of data are seen to overlap where the substrate phase roughness heights are large and differ by nearly 50% for the low phase roughness mask areas. Fixed uncertainty at 10% is assumed for both sets of data.

# III. ACTINIC MASK SURFACE IMAGING

The SEMATECH Berkeley Actinic Inspection Tool (AIT) is a dual-mode EUV microscope used for mask inspection at the operating wavelength of 13.4nm. Details of the system can be found in the literature[24, 25]. In the imaging mode, the AIT operates as a high resolution, zoneplate based EUV microscope designed to emulate EUVL stepper systems. Flare in the AIT is given to be 2-3% [24], the illumination partial coherence is found to be below 0.2, and the major aberrations in the system are shown to be astigmatism combined with focal plane tilt and coma [25].

In the imaging mode, the zoneplate projects a 907× magnified image of the illuminated area on mask on to a back illuminated, 1x1inch square, EUV charge coupled device (CCD) camera. Though-focus series of images for four different regions at specific points along the rough gradient were collected with a 0.3NA, 4x stepper equivalent zoneplate. Each image collected in the series is a 16 bit, 2048 x 2048 array corresponding to a 30µm square area on the mask. Analysis of each image is completed to extract the appropriate speckle contrast in the image.

The full image area of the mask collected with the AIT CCD camera is not usable for analysis due to illumination non-uniformities and aberrations. The part of the image where the imaging can be considered diffraction limited is small compared to overall image size and needs to be identified for each image. Analysis of each image area is completed by dividing the image into 256 arrays of 128 x 128 pixels that correspond to an area of $3.7\mu m^2$ on the mask. Further corrections to the sub-arrays are completed with removing the mean background and by removing the image plane tilts by dividing each sub-array by its best-fit plane. For the rough mask surfaces imaged, the contrast of the granularities seen in the images are determined by computing the normalized standard deviations of the image intensities at the nearly diffraction limited area of each image.

Figure 7 gives an example of a typical set of image series through focus collected for a single multilayer window. The corresponding speckle contrast is also shown directly below each image in the series. The contrast of the roughness related granularities in the image is found to be a minimum at the best focus condition of the lens. The speckle contrast observed at the best focus of each set of data is plotted against the region number in figure 8. The adjacent table provides contrast data as well as the corresponding phase roughness determined from the AFM measurements. Even at the smallest roughness scale, a speckle contrast better than 6% is observed.

**Figure 7:** An image series through focus, collected for a single multilayer rough window using the AIT zone-plate EUV microscope. The corresponding speckle contrast, which is just the normalized standard deviation of the image intensities, is also shown for each image in the series.

**Figure 8:** The speckle contrast observed at the best focus of each rough surface data collected is shown. The adjacent table provides contrast data as well as the corresponding phase roughness determined from the AFM measurements. Even at the smallest roughness scale, a speckle contrast better than 6% is observed.

# IV. SIMULATIONS

The question that is central to this paper is, if indirect top surface phase roughness characterizations can be trusted explicitly for predicting scatter related speckle in the image field. In order to determine the effectiveness of surface characterizations, we try to reproduce the image plane speckle determined from the AIT images by modeling the rms roughness content obtained with the AFM and XRS.

AIT imaging characteristics are modeled with a 2-D, scalar, aerial image computation software developed in-house. Scalar modeling and thin mask approximation is appropriate for the small NA's that are being used here[9, 26]. The rough mask synthesized from the AFM image PSDs containing the phase error content is modeled as a pure phase distribution. The phase is

determined from the geometric path length differences, under the assumption that EUV light to be reflected from the top surface of the mask.

Initial calculations were completed under the assumption that the AIT images are diffraction limited; this yielded speckle contrast values that were far from the AIT measured speckle. Subsequent calculations are completed including the AIT design aberrations. AIT design aberrations are computed for a 2µm field using raytracing methods and tabulated in table 3. Astigmatism and defocus are found to be the dominant Zernike terms in the system. Additionally, a 2.5% coherent optics produced scatter reported for the AIT is added in quadrature to the modeled speckle contrast at best focus.

**Table 3:** AIT design aberrations are computed for a 2µm field using raytracing. Astigmatism and defocus are found to be the dominant Zernike terms in the system.

The calculated speckle contrast based on the AFM measured roughness data is compared to the measured speckle, which is shown in Figure 9. AIT image based contrast does not match completely to the calculated values and a crossover point is observed near the high roughness regions. This is observed to be consistent through many simulation sets. When compared to XRS roughness data simulations, the AFM is shown to be a better fit to the measured images. The plot of all data is given in figure 10 and the corresponding data points are tabulated in table 4. All data is shown to overlap in the taller phase error conditions.

**Figure 9:** The calculated speckle contrast based on the AFM measured roughness data is compared to the measured speckle. AIT image based contrast does not match completely to the calculated values and a crossover point is observed near the high roughness regions.

**Figure 10:** Calculated image contrast for AFM and XRS determined phase roughness as compared to the measured image contrast. When compared to XRS roughness data simulations, the AFM is shown to be a better fit to the measured images.

**Table 4:** Comparing measured and simulated image speckle contrast. Simulations are based on the rms roughnesses obtained from the AFM images and the XRS reflectance.

## V. Discussion

In this paper, we try to systematically study the effects of substrate roughness on image plane speckle. Surface metrology was completed with AFM and X-ray reflectometry. The AFM and XRS based measurements of the rms phase roughness are observed to differ in the small roughness ranges characteristic of the EUV mask substrates fabricated at present. Speckle analysis was completed using the AIT EUV imaging microscope. Furthermore, we predict the measured image plane speckle contrast from the two different roughness metrologies in order to determine the most effective EUV mask roughness metrology. XRS calculated roughness based modeled data is shown to deviate further from the measured speckle contrasts in small roughness regime.

We attribute the XRS departure from the AFM measurements to two reasons. The first source of error is expected to be in the initial reflectivity chosen for XRS roughness calculations.

It is an average of the reflectivities obtained for the first few rough surface regions in the very low roughness region. Ideally we would want the initial reflectivity measurement to be free of any roughness at all. The second major error comes from ignoring the absorption of the incident beam on sample surface.

For a better roughness metrology, we plan to measure total integrated scatter and compare the scatter power spectral density information to the AFM image scans. We expect that the total integrated measurements will be a much more accurate method for determining the true roughness of the mask substrate. Further evaluations using resist exposures of the patterned rough areas with the SEMATECH Berkely 0.3NA MET[27] are being planned.

## Acknowledgments

We acknowledge SEMATECH for the support of the SEMATECH Berkeley MET and AIT; in particular, the programmatic support from Warren Montgomery, Bryan Rice, and Stefan Wurm. This work was supported in part by SEMATECH and carried out at Lawrence Berkeley National Laboratory's Advanced Light Source, which is supported by the DOE, Office of Science, and the Basic Energy Sciences under contract no. DE-AC02-05CH11231.

[1]R.H. Stulen and D.W. Sweeney, IEEE J. Quant. Elec. **35,** 694 (1999).

[2] V. Bakshi, *EUV Lithography* (SPIE Press, Washington, 2007).

[3]B. Wu and A. Kumar, *Extreme Ultraviolet lithography* (The McGraw Hill Companies, inc., San Francisco, 2009).

[4]B. LaFontaine, A. R. Pawloski, Y. Deng, C. Chovino, L. Dieu, O. R. Wood, II, and H. J. Levinson, Proc. SPIE **5374,** 300 (2004), and references therein.

[5]E. Spiller, *Soft X-ray Optics* (SPIE Optical Engineering Press, Washington, 1994).

[6]J. A. R. Samson and D. L. Ederer, *Vacuum Ultraviolet Spectroscopy volume 1* (Academic Press, San Diego, 1998).

[7]D. Stearns and E. Gullikson, "Nonspecular scattering from extreme ultraviolet multilayer coatings," Physica B 283, 84-91 (2000).

[8]D. G. Stearns, D. P. Gaines, D. W. Sweeney, and E. M. Gullikson, J. Appl. Phys. **84**, 1003 (1998).

[9]J. W. Goodman, Statistical Optics (Wiley, New York, 1985.

[10]N. Beaudry and T. Milster, "Effects of object roughness on partially coherent image formation," Opt. Lett. 25, 454-456 (2000).

[11]International Technology Roadmap for Semiconductors, 2009 ed., http://www.itrs.net/

[12]R. Brainard, C. Henderson, J. Cobb, V. Rao, J. Mackevich, U. Okoroanyanwu, S. Gunn, J. Chambers, and S. Connolly, J. Vac. Sci. Technol. B 17, 3384–3389 (1999).

[13] G. Gallatin, Proc. SPIE **5754**, 38-52 (2005).

[14]P. P. Naulleau and G. Gallatin, J. Vac. Sci. Technol. B 26, 1903 (2008), and references therein.

[15]P. P. Naulleau, D. Niakoula, and G. Zhang, J. Vac. Sci. Technol. B 26, 1289 (2008).

[16]P. Naulleau, Appl. Opt. 48, 3302-3307 (2009).

[17]T. Liang, E. Ultanir, G. Zhang, S.-J. Park, E. Anderson, E. Gullikson, P. Naulleau, F. Salmassi, P. Mirkarimi, E. Spiller, and S. Baker, J. Vac. Sci. Technol. B 25, 2098 (2007).

[18]T. Pistor, T. Y. Deng, and A. Neureuther, "Extreme ultraviolet mask defect simulation: Low-profile defects," J. Vac. Sci. Technol. B 18, 2926-2929 (2000).

[19] P. P. Naulleau and S. A. George, Proc. SPIE 7379, 73790O (2009.

[20]P. P. Naulleau, S. A. George, and B. M. McClinton, Proc. SPIE 7636, 76362H (2010).

[21]H. Kinoshita, T. Watanabe, A. Ozawa, and M. Niibe, Proc. SPIE **3412,** 358 (1998).

[22]SuMMIT Software Division of EUV Technology, *Summit Litho Image Analysis Software*, 2009. http://www.euvl.com/summit/

[23]E. M. Gullikson, S. Mrowka, and B. B. Kaufmann, in Emerging Lithographic Technologies V, E. A. Dobisz ed., Proc. SPIE **4343**, 363 (2001).

[24]K. A. Goldberg, P. P. Naulleau, Anton Barty, S. B. Rekawa, C. D. Kemp, R. F. Gunion, F. Salmassi, E. M. Gullikson, E. H. Anderson, and H.-Seung Han, Proc. SPIE 6730, 67305E (2007).

[25]K. A. Goldberg, I. Mochi, P. Naulleau, T. Liang, P.-Y. Yan, and S. Huh, J. Vac. Sci. Technol. B 27, 2916 (2009), and references therein.

[26]E. Gullikson, C. Cerjan, D. Stearns, P. Mirkarimi, and D. Sweeney, "Practical approach for modeling extreme ultraviolet lithography mask defects," J. Vac. Sci. Technol. B 20, 81-86 (2002) .

[27]P. P. Naulleau, C. N. Anderson, L-M Baclea-an, D. Chan, P. E. Denham, S. A. George, K. A. Goldberg, B. Hoef, G. Jones, C. Koh, B. La Fontaine, B. McClinton, R. Miyakawa, W. Montgomery, S. Rekawa, and T. Wallow, Proc. SPIE 7636, 76361J (2010).

# List of Tables

Table 1: Roughness (root mean squared deviations) computed from AFM imaged surface profiles before and after the multilayer depositions.

Table 2: Comparison of rms roughness computed from AFM imaging and XRS reflectance

Table 3: AIT design aberrations computed for a 2µm field using raytracing. Astigmatism and defocus are found to be the dominant Zernike terms in the system.

Table 4: Comparing measured and simulated image speckle contrast. Simulations are based on the rms roughnesses obtained from the AFM images and the XRS reflectance.

Table 1:

| **Window Number** | **Chrome Surface [nm rms]** | **Chrome Surface with Multilayer[nm rms]** |
|---|---|---|
| 6 | 0.23 | 0.2 |
| 7 | 0.3 | 0.27 |
| 8 | 0.47 | 0.32 |
| 10 | 0.59 | 0.43 |
| 11 | 0.57 | 0.45 |
| 12 | 0.63 | 0.47 |
| 13 | 0.6 | 0.46 |
| 14 | 0.68 | 0.48 |
| 15 | 0.8 | 0.49 |
| 16 | 0.73 | 0.52 |
| 18 | 0.68 | 0.54 |

**Table 2:**

| Window Number | XRS roughness [nm rms] | AFM roughness [nm rms] |
|---|---|---|
| 6 | 0.10 | 0.2 |
| 7 | 0.13 | 0.27 |
| 8 | 0.23 | 0.32 |
| 9 | 0.30 | n/a |
| 10 | 0.36 | 0.43 |
| 11 | 0.41 | 0.45 |
| 12 | 0.44 | 0.47 |
| 13 | 0.46 | 0.46 |
| 14 | 0.48 | 0.48 |
| 15 | 0.49 | 0.49 |
| 16 | 0.50 | 0.52 |
| 17 | 0.51 | n/a |
| 18 | 0.52 | 0.54 |

**Table 3:**

| | Field location (x,y) um | | | | | | | | | |
|---|---|---|---|---|---|---|---|---|---|---|
| Zernike Numbers | 0.0,0.0 | 0.0,0.5 | 0.0,1.0 | 0.5,0.0 | 0.5,0.5 | 0.5,1.0 | 1.0,0.0 | 1.0,0.5 | 1.0,1.0 | Field-weighted average |
| Z3 (Defocus) | -0.0017 | -0.0161 | -0.0305 | -0.0017 | -0.0161 | -0.0304 | -0.0016 | -0.0160 | -0.0303 | **-0.0189** |
| Z4 (Astig. 90) | 0.0012 | 0.0155 | 0.0297 | 0.0013 | 0.0156 | 0.0298 | 0.0014 | 0.0157 | 0.0299 | **0.0184** |
| Z5 (Astig. 45) | 0.0000 | 0.0000 | 0.0000 | -0.0144 | -0.0143 | -0.0142 | -0.0288 | -0.0286 | -0.0285 | **-0.0172** |
| Z6 (Coma X) | 0.0000 | 0.0000 | 0.0000 | 0.0040 | 0.0040 | 0.0040 | 0.0080 | 0.0080 | 0.0080 | **0.0048** |
| Z7 (Coma Y) | 0.0014 | 0.0052 | 0.0091 | 0.0014 | 0.0052 | 0.0091 | 0.0014 | 0.0052 | 0.0091 | **0.0060** |
| Z8 (Spherical) | -0.0002 | -0.0002 | -0.0001 | -0.0002 | -0.0002 | -0.0001 | -0.0002 | -0.0002 | -0.0001 | **-0.0002** |
| Weight | 1 | 2 | 2 | 2 | 4 | 4 | 2 | 4 | 4 | |

**Table 4:**

| Window Number | AIT measured speckle contrast (%) | 2D Modeled (AFM rms) speckle contrast (%) | 2D Modeled (XRS rms) speckle contrast (%) |
|---|---|---|---|
| 1 | 6.8 | 5.1 | 3.5 |
| 6 | 8.9 | 6.6 | 3.2 |
| 10 | 10.7 | 9.9 | 8.3 |
| 14 | 12 | 12.8 | 12.7 |

# List of Figures

Figure 1: A grid pattern of windows sized 1x3mm and separated by 1.5mm, going from low roughness to high roughness. There are a total of 18 windows sized 1x3mm and separated by 1.5mm in the row that was evaluated for this study. The clear multilayer surface is inside the window and resist absorber giving full attenuation of EUV is on the outside. .............................. 3
Figure 2: Root mean square height deviations from the AFM surface profiles of the sputter coated Chrome on Si rough mask, before and after Mo/Si multilayer coating. Rougher areas of the mask show smoothing after multilayer is deposited and at smaller roughness scales, the smoothing appears to be diminished.......................................................................................... 3
Figure 3: PSDs generated (window 6, top) in the low roughness region with the solid black curve is the PSD of the chromium surface by itself. An increase in the low spatial frequency range (LSFR) and some smoothing into the mid to high spatial frequencies (MSFR and HSFR) are observed after the ML is coated on this surface. In contrast, the PSD's for high roughness (window 15, bottom) show significant reduction into all frequencies after ML deposition. The taller phase structures are assumed to have been smoothed. .......................................................... 4
Figure 4: Images synthesized from AFM image scans to be used for the thin mask model for predicting phase coherent roughness contributed speckle. ............................................................ 4
**Figure 5:** The reflectance and scattering yields for the measurements from the different windows are shown on the scale of increasing roughness. Increase in scattering follows the decrease in reflectance, indicating an increase in phase roughness. Wavelength of light used was 13.46 nm at a 5 degree angle of incidence for reflectance relative to the normal. The scattering was obtained at a fixed angle that was 10 degrees away from the normal. .................................... 4
Figure 6: AFM and XRS measured rms roughness are compared. The two sets of data are seen to overlap where the substrate phase roughness heights are large and differ by nearly 50% for the low phase roughness mask areas. Fixed uncertainty at 10% is assumed for both sets of data. ....... 5
Figure 7: An image series through focus, collected for a single multilayer rough window using the AIT zone-plate EUV microscope. The corresponding speckle contrast, which is just the normalized standard deviation of the image intensities, is also shown for each image in the series. ....................................................................................................................................... 6
Figure 8: The speckle contrast observed at the best focus of each rough surface data collected is shown. The adjacent table provides contrast data as well as the corresponding phase roughness determined from the AFM measurements. Even at the smallest roughness scale, a speckle contrast better than 6% is observed. ......................................................................................... 6
Figure 9: The calculated speckle contrast based on the AFM measured roughness data is compared to the measured speckle. AIT image based contrast does not match completely to the calculated values and a crossover point is observed near the high roughness regions. ................... 7
Figure 10: Calculated image contrast for AFM and XRS determined phase roughness as compared to the measured image contrast. When compared to XRS roughness data simulations, the AFM is shown to be a better fit to the measured images. ......................................................... 7

# Extreme ultraviolet mask substrate surface roughness effects on lithographic patterning

**Figure 1:**

**Figure 2:**

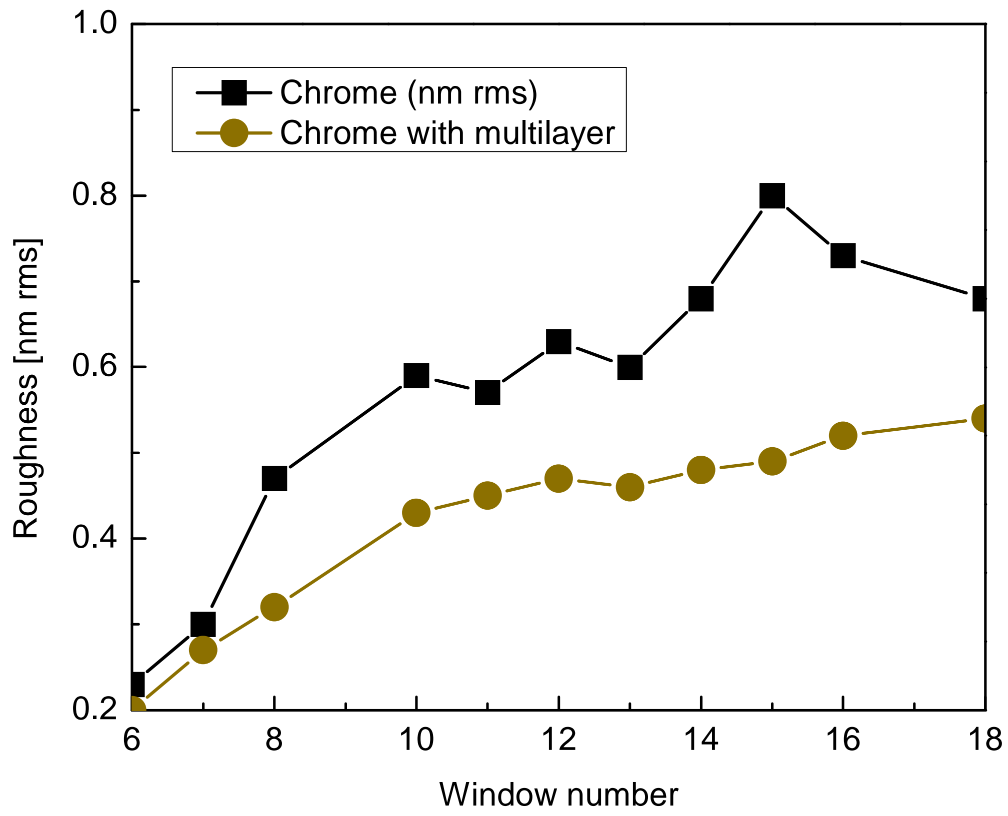

**Figure 3:**

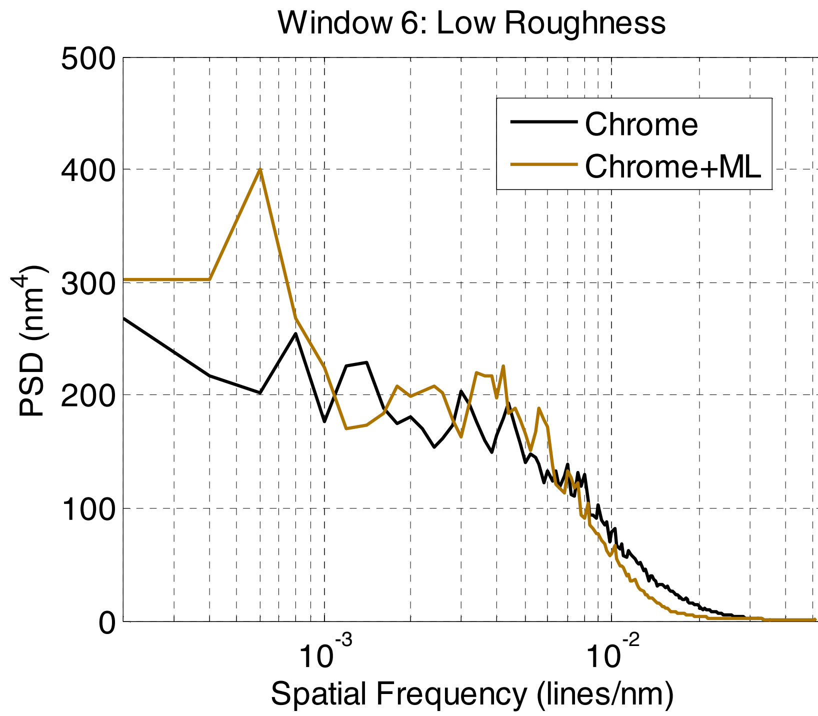


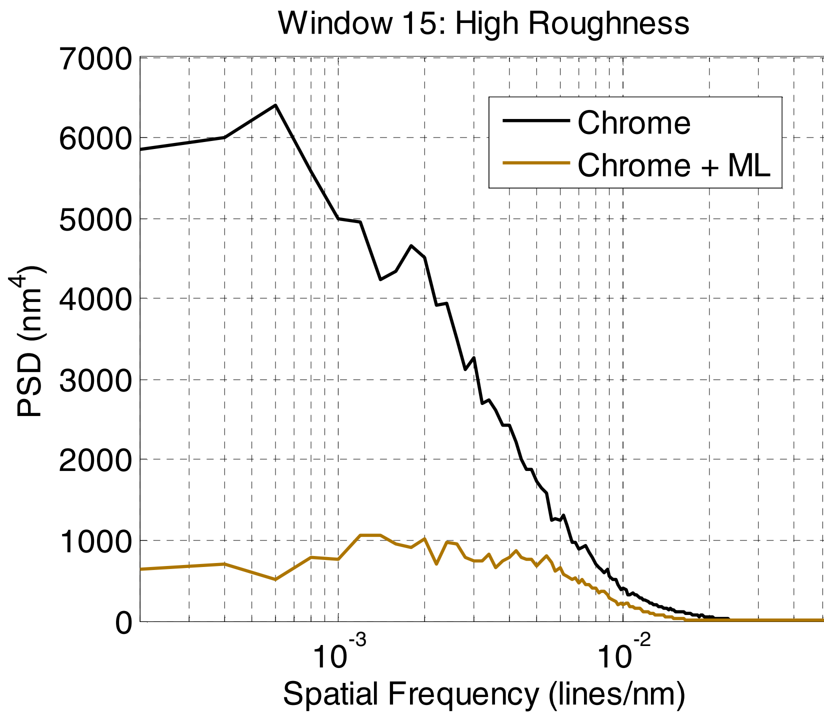

**Figure 4:**

A. Small phase roughness (0.2 nm)

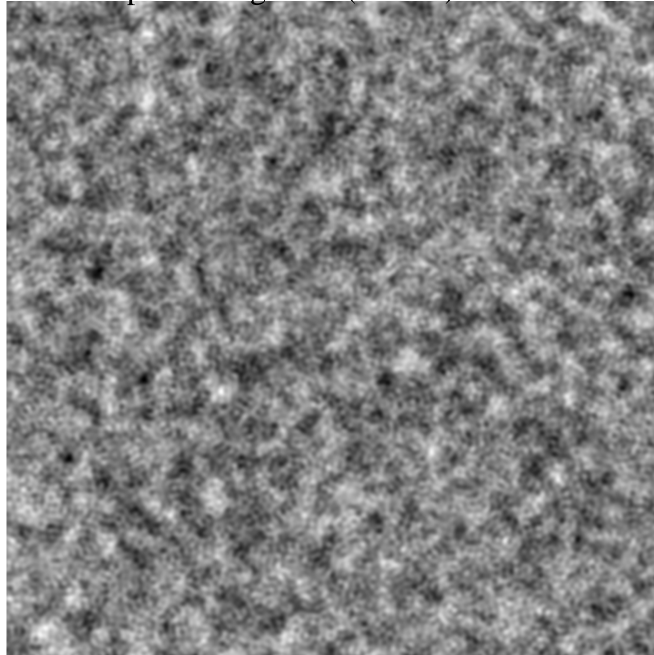

B. High phase roughness (0.5 nm)

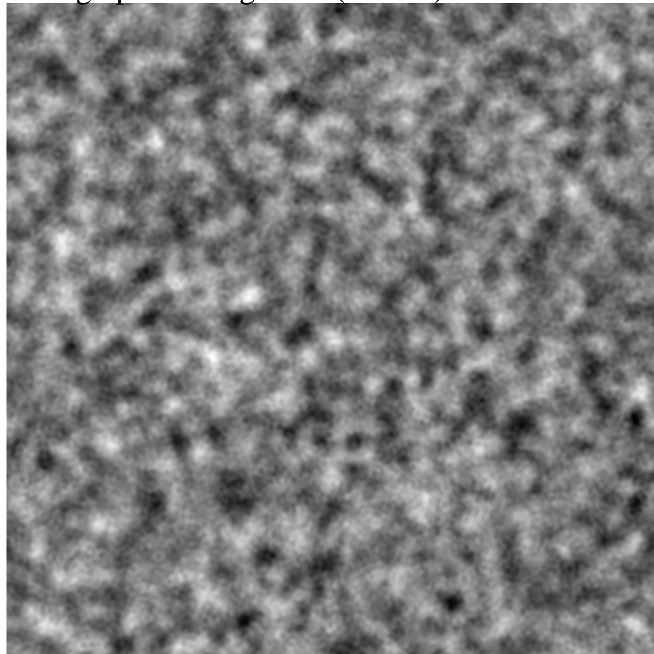

**Figure 5:**

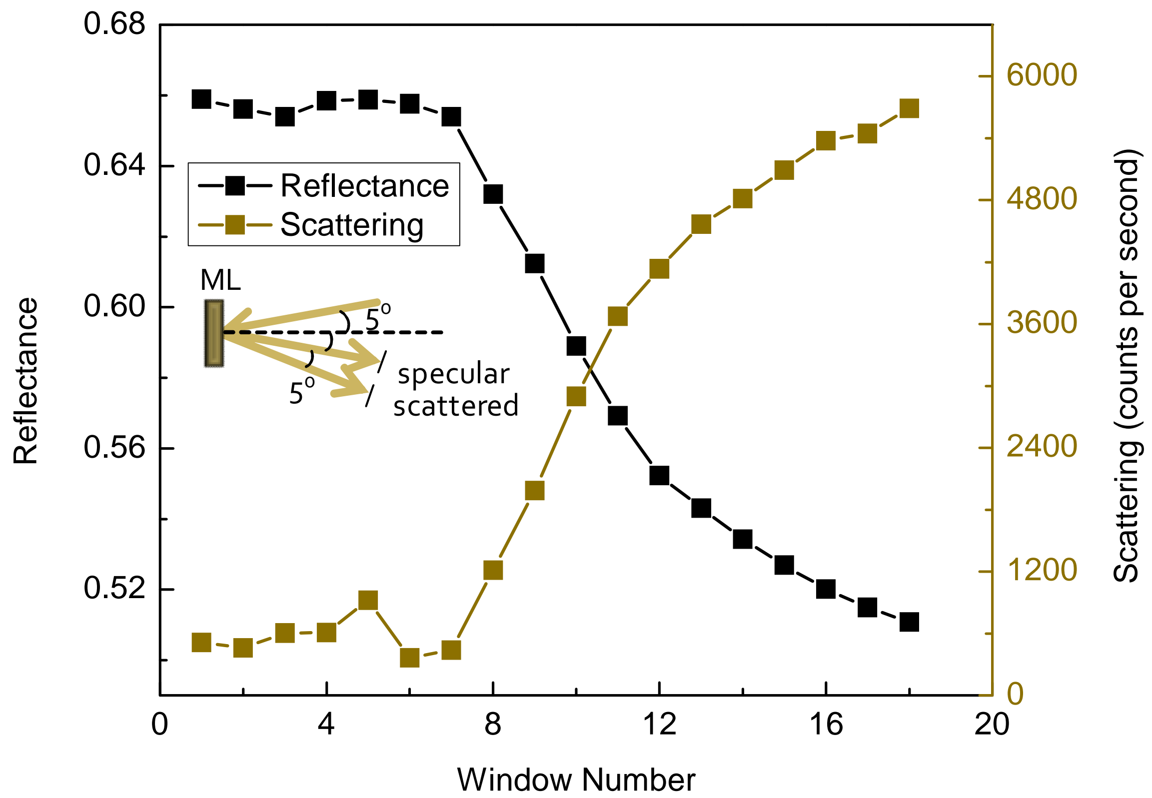

**Figure 6:**

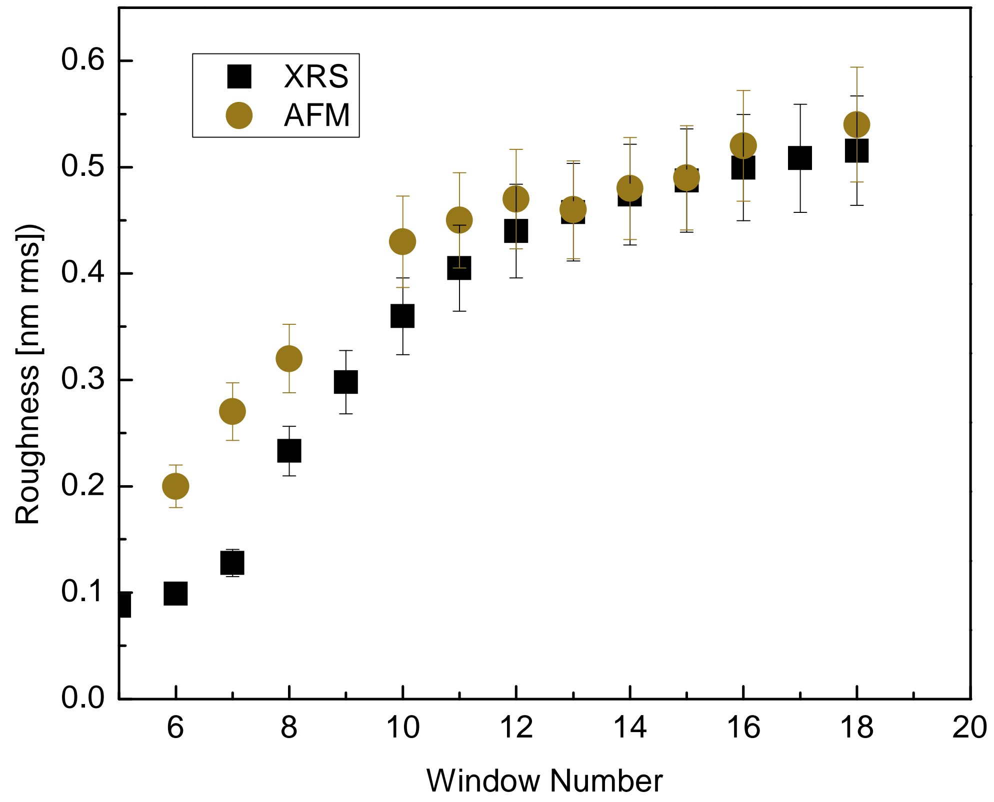

**Figure 7:**

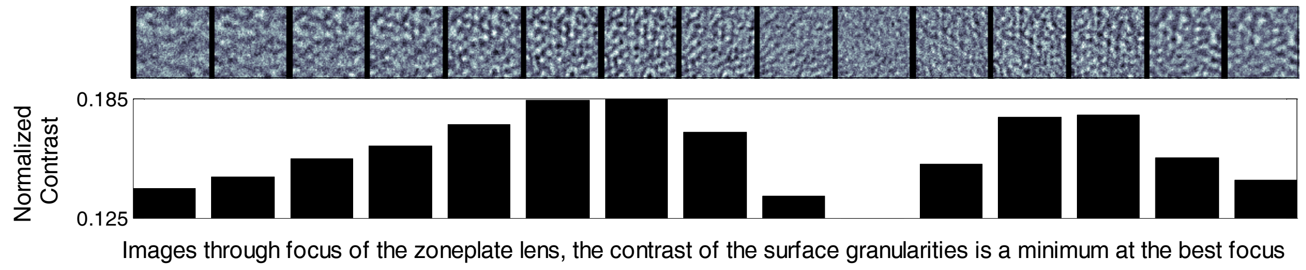


Images through focus of the zoneplate lens, the contrast of the surface granularities is a minimum at the best focus

**Figure 8:**

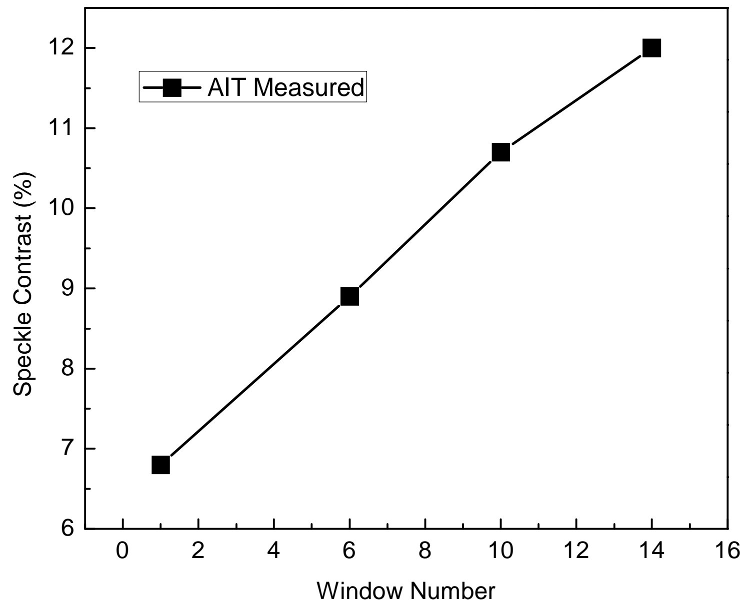


0.3NA equivalent zone plate, FOV – 1μm

| Window | AIT | AFM [nm rms] |
|---|---|---|
| 1 | 6.8 | 0.16 |
| 6 | 8.9 | 0.20 |
| 10 | 10.7 | 0.32 |
| 14 | 12.0 | 0.46 |
| 18 | NA | 0.54 |

**Figure 9:**

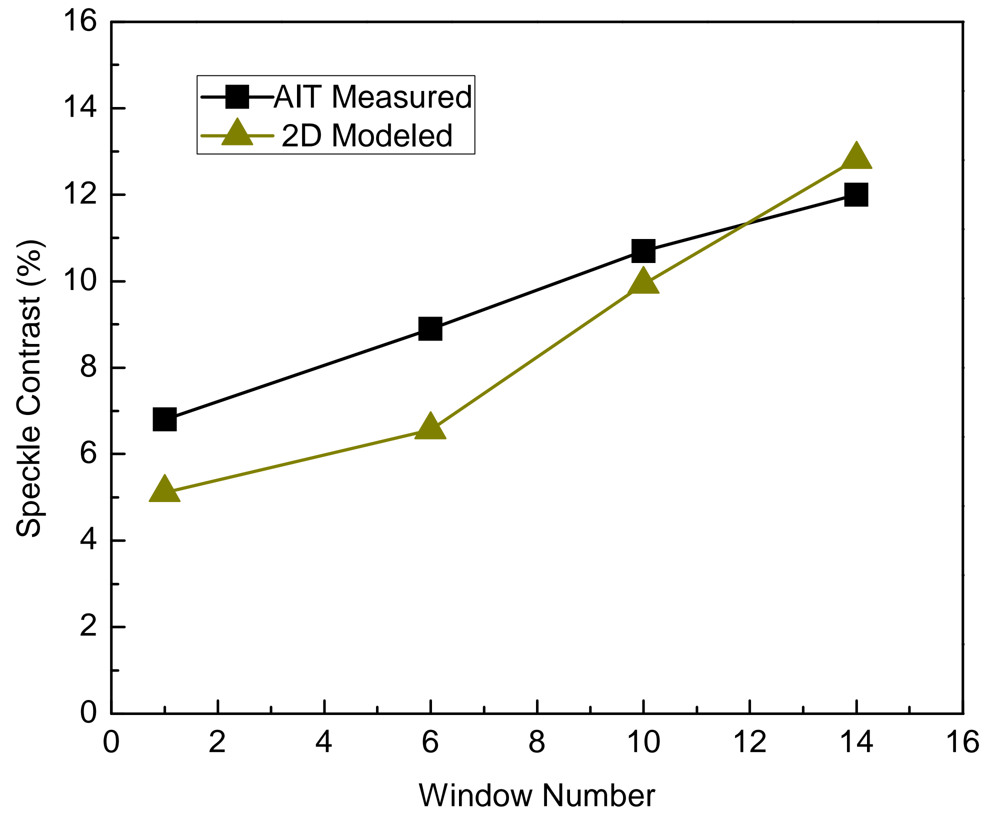

**Figure 10:**